RSC Advances

ROYAL SOCIETY OF CHEMISTRY

PAPER

View Article Online
View Journal | View Issue

Check for updates

Cite this: *RSC Adv.*, 2026, **16**, 24997

Fe doped ZnO nanomaterials for energy storage applications as high-capacitance supercapacitor electrodes

Srikanth R. Veerabhadraiah,[a] Gowri Soman,[b] Sachin A. Bhat,[c] Rohit K. Sharma,[c] Ravikumar Thimmappa,[d] Chinmaya Mirle,[e] Gurumurthy Hegde,*[bf] C. V. Yelamaggad[c] and Nagaraja Naik*[a]

Received 21st March 2026
Accepted 4th May 2026

DOI: 10.1039/d6ra02336c

rsc.li/rsc-advances

Enhancing the performance of electrode materials is essential for developing high-capacitance supercapacitors, and transition-metal-doped metal oxides have shown particular promise in this regard. In this work, Fe-doped ZnO nanostructures were synthesized using a sonochemical method and systematically examined through XRD, SEM, TEM, XPS and UV–vis analyses to verify Fe incorporation and the resulting changes in crystallinity, morphology and optical behaviour. The structural modifications induced by Fe were evident in the electrochemical response, with the optimized ZnO–Fe sample delivering a specific capacitance of 11.4 F g^{-1} at 0.1 A g^{-1} in the two-electrode system and 462 F g^{-1} in the three-electrode system, both measured in 3 M KOH electrolyte. A CR2032 coin cell assembled with this material achieved an energy density of 1.6 Wh kg^{-1} and a power density of 2890.93 W kg^{-1}, demonstrating an effective balance between energy storage and power output. These findings highlight the suitability of Fe-doped ZnO as a tunable electrode material and support its further exploration in advanced supercapacitor systems.

1. Introduction

The increasing global demand for efficient and sustainable energy storage systems is driven by the rapid advancements in renewable energy technologies and the necessity for reliable power sources.[1,2] Energy storage is critical in stabilizing power grids, improving energy efficiency, and enabling the widespread adoption of renewable energy solutions. Supercapacitors have emerged as promising alternatives to conventional batteries among various energy storage technologies due to their unique combination of high power density, long cycle life, and rapid charge–discharge capabilities.[3–6] These attributes make them particularly suitable for applications requiring quick energy bursts, such as electric vehicles, portable electronics, and grid stabilization.[7,8] Supercapacitors, also known as electrochemical capacitors, bridge the gap between traditional capacitors and batteries by offering both high energy storage and fast charge–discharge rates.[3–8] Unlike batteries, which rely on faradaic redox reactions for energy storage, supercapacitors primarily store charge electrostatically in electric double-layer capacitors (EDLCs)[9] or through surface redox reactions (pseudocapacitors).[10] EDLCs utilize carbon-based materials with high surface areas to achieve physical charge separation at the electrode–electrolyte interface. Pseudocapacitors employ transition metal oxides or metal organic frameworks[11,12] to enable reversible redox reactions at the electrode surface. This mechanism allows supercapacitors to achieve a significantly longer lifespan and deliver high power within short time frames. These advantages make supercapacitors superior to batteries in applications where rapid energy delivery and extended durability are essential.

To further enhance the energy density of supercapacitors while maintaining their power capabilities, extensive research has focused on developing advanced electrode materials. Zinc oxide (ZnO) has garnered significant attention as a promising material for supercapacitor electrodes due to its unique properties, including a wide bandgap (~3.3 eV), high electron mobility (115–155 cm^2 V^{-1} s^{-1}), and environmental friendliness.[13] ZnO exhibits excellent electrochemical stability and good conductivity while being abundantly available. It can facilitate both electric double-layer capacitance (EDLC) and pseudo capacitance mechanisms, enhancing its overall charge storage capability. Additionally, its high surface area and

---

[a] Department of Studies in Chemistry, Manasagangotri, University of Mysore, Mysuru 570006, India. E-mail: drnaikchem@gmail.com

[b] Department of Chemistry, Christ University, Hosur Road, Bengaluru 560029, India. E-mail: murthyhegde@gmail.com

[c] Centre for Nano and Soft Matter Sciences, Bengaluru 562162, India

[d] Department of Energy Science and E-Mobility, Atria University, Bengaluru 560024, India

[e] Institute of Organic and Macromolecular Chemistry, Ulm University, Albert-Einstein-Allee11, 89081 Ulm, Germany

[f] Department of Chemistry, B. N. M. Institute of Technology, Banashankari, Bengaluru, 560070, Karnataka, India

tunable morphology contribute to improved electrochemical performance. For instance, ZnO nanostructures such as nanorods and nanosheets have demonstrated enhanced ion accessibility and charge transfer kinetics. Despite these advantages, pure ZnO suffers from several limitations that hinder its widespread adoption in supercapacitor applications. Its relatively low intrinsic conductivity restricts charge transport efficiency and reduces rate capability. Furthermore, significant volume changes during charge–discharge cycling lead to structural degradation and reduced long-term stability. The dissolution and aggregation of ZnO nanoparticles in electrolyte solutions further compromise cycling stability over extended usage. These challenges necessitate material modifications to improve electrical conductivity, structural integrity, and overall electrochemical performance.

Doping with metals has emerged as an effective strategy to overcome its inherent limitations and enhance its suitability for supercapacitor applications.[14–22] Transition metal doping introduces localized electronic states in ZnO that enhance electrical conductivity and electrochemical activity by modifying its band structure and creating defect sites, such as oxygen vacancies. Various dopants including cobalt, nickel, manganese, and iron—have been explored to optimize the electrochemical performance of ZnO. Doped ZnO materials exhibit improved charge storage capacity, enhanced ion diffusion rates, and better structural stability compared to undoped ZnO. Among these dopants, iron (Fe) has shown particular promise in improving the electrochemical properties of ZnO for supercapacitor applications. Fe doping modifies the electronic structure of the oxide nanoparticle by introducing oxygen vacancies within the lattice framework while reducing its bandgap. These vacancies act as efficient charge transport pathways that enhance conductivity and ion diffusion kinetics. Additionally, Fe^{3+} ions create localized electronic states that enable reversible redox transitions between Fe^{2+} and Fe^{3+} ions at the electrode surface, significantly augmenting pseudo capacitive charge storage mechanisms. For example, 3% Fe-doped ZnO nanostructures synthesized *via* microwave irradiation have demonstrated a specific capacitance of 286 F g^{-1} at 10 mV s^{-1}, a 58% improvement over undoped ZnO, alongside 85% capacitance retention over 2000 cycles due to stabilized nanostructures *via* magnetic polaron interactions.[23] The doping concentration critically influences performance, while low Fe concentrations (1 to 3 wt%) optimize capacitive behaviour by balancing defect creation with structural stability, higher concentrations (>5 wt%) risk nanoparticle aggregation or phase segregation that degrades cyclability. Morphological control also plays a pivotal role, Fe doping promotes rod- and nanosheet-like structures with high surface areas, enhancing ion accessibility and redox-active sites.

Among various methods[23–25] to synthesise doped zinc oxide nanomaterials, sonochemical synthesis has proven to be a promising technique due to its ability to produce different morphologies and sizes of nanomaterials, and its rapid reaction rates,.[26] In this study, we explore the synthesis of Fe-doped ZnO nanostructures using a sonochemical technique, which builds up on our previous work,[27,28] here we investigate the structural, morphological, magnetic, and electrochemical properties of Fe doped ZnO nanomaterials, with a particular focus on their performance as electrode materials for supercapacitors. Our goal is to achieve high specific capacitance and excellent cycling stability with minimal Fe doping, thereby optimizing the material's performance for energy storage applications. By systematically varying the Fe concentration, we aim to understand the relationship between doping levels and the resulting electrochemical properties, ultimately contributing to the development of advanced supercapacitor materials.

2. Materials

Zinc acetylacetonate hydrate [$Zn(C_5H_7O_2)_2\ H_2O$], iron (III) acetylacetonate [$Fe(C_5H_7O_2)_3$] and ethanol were procured from Merck-Sigma-Aldrich, India, and sodium hydroxide [NaOH] was procured from Sisco Research Labs, India. All chemicals were of analytical grade. Deionized water from the Millipore Mill-Q system was used for synthesis.

2.1. Sonochemical synthesis of Fe doped ZnO nanomaterials

For the sonochemical reaction, 125 mL aqueous NaOH solution of 0.1 M was added dropwise to 125 mL aqueous ethanolic solution (1 : 1.5 of EtOH : H_2O) containing 0.05 M [$Zn(acac)_2\ H_2O$] and various concentrations of [$Fe(C_5H_7O_2)_3$] (0.5, 1.0, 2.0, 3.0 and 5.0 wt%) under constant stirring. Stirring continued for 30 min, the pH of the mixture of two solutions found to be ∼10–11. The resultant solution was subjected to ultrasonic irradiation in the sonicator bath [Branson M 1800, 40 ± 1 kHz] for 1 h. The temperature of the reaction mixture rose up to 60 °C. The obtained solution containing precipitate was centrifuged for 10 min at 12 000 rpm and resultant powder was collected and air dried at room temperature. Fe doped ZnO nanomaterials synthesised by adding 0.5, 1.0, 2.0, 3.0 and 5.0 wt% of [$Fe(C_5H_7O_2)_3$] referred as ZnO–$Fe_{0.5\%}$, ZnO–$Fe_{1.0\%}$, ZnO–$Fe_{2.0\%}$, ZnO–$Fe_{3.0\%}$, and ZnO–$Fe_{5.0\%}$ respectively (Scheme 1).

2.2. Characterisation methods for Fe doped ZnO nanomaterials

Fe doped ZnO nanomaterials crystal structure was characterized by powder X-ray diffraction (XRD, Rigaku smart lab powder diffractometer with monochromatic Cu kα radiation). Fe doped ZnO nanomaterials dispersed in ethanol and used for room temperature UV–visible absorption measurements using UV–vis spectrophotometer (Thermo Scientific Genesys 180). The FT-IR (Fourier Transform Infra-Red) spectra were recorded using PerkinElmer spectrum with KBr pellet technique. Raman spectroscopic analysis was obtained using Renishaw inVia Raman Microscope. The morphology, size, shape and elemental composition was analysed using field emission scanning electron microscopy (FESEM) TESCAN, MIRA equipped with energy dispersive X-ray (EDX) detector (Bruker, Quantax 200) and Transmission electron microscopy (TEM) analysis using Thermofisher, Talos F200 S. Thermal behaviour was investigated using NETZSCH STA 2000 TGA/DTA instrument. X-ray photoelectron spectroscopic (XPS) analysis was performed using

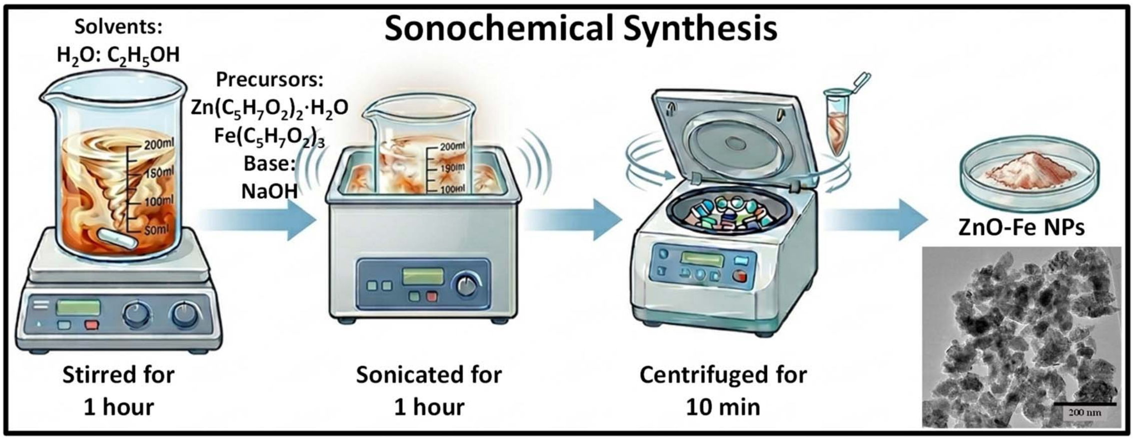

Scheme 1 Sonochemical synthesis of Fe doped ZnO nanomaterials.

Specs XPS system with a Phoibos 150 energy analyser. The spectra were recorded using monochromatized Al Kα radiation (200 W, 12 kV). The peak fit of the XPS results was done with CasaXPS, using Shirley-type backgrounds and Gaussian–Lorentzian (GL30) peak shapes.

2.3. Fabrication of coin-cell electrodes

For the fabrication of symmetric supercapacitor electrodes, nickel foam was first cut into circular discs of the desired size and thoroughly cleaned. A suspension of 6 mg of the active material in ethanol was prepared and uniformly drop-cast onto the pre-cut nickel foam. The coated foams were dried to evaporate the solvent, followed by gentle pressing to ensure good contact between the active material and the current collector. After drying and weighing to confirm the active material loading, two identical electrodes, along with a separator and the chosen electrolyte, were assembled into a CR2032 coin cell and crimped for electrochemical measurements.

2.4. Electrochemical measurements

The working electrode was prepared by coating a homogeneous slurry of active material (*i.e.*, ZnO–$Fe_{0.5\%}$, ZnO–$Fe_{1.0\%}$, ZnO–$Fe_{2.0\%}$, ZnO–$Fe_{3.0\%}$, and ZnO–$Fe_{5.0\%}$) along with polyvinylidene fluoride (PVDF) as binder and carbon black as conductive additive in 90%: 5%; 5% respectively in Ni foam (1.5 mm thickness) with NMP (*N*-methyl-2-pyrrolidone) as solvent. Nickel foam is chosen as the current collector due to its conductivity and its mechanically robust 3D porous structure ensures low internal resistance, good electrolyte access, and strong adhesion of active materials.[29] Prior to electrode preparation, Ni foam underwent a cleaning procedure to ensure a contamination-free and active surface. The foam was first treated with 0.1 M HCl for 30 minutes at room temperature to remove surface oxides and improve wettability. It was then sonicated in deionized water for 15 minutes, followed by sonication in ethanol for 15 minutes to remove any residual contaminants. After cleaning, the foam was dried at 60 °C. This process ensures a clean, reactive surface, promoting better adhesion of the deposited material and enhancing the reliability of the electrochemical measurements.[30] A calomel electrode is employed as the reference electrode and a platinum wire as the counter electrode in 3 M KOH as the electrolytic solution. The 3 M KOH electrolyte is commonly used as it provides an optimal balance of ionic conductivity, electrode–electrolyte interaction, and chemical stability for Fe-doped ZnO electrodes. Higher or lower concentrations typically reduce ion mobility or introduce instability, making 3 M the most effective choice for reliable supercapacitor performance.[31] The fabricated electrodes were taken up for electrochemical investigations. The electrochemical performance of the synthesized samples were tested with the help of MetrohmAutolab M302 with techniques such as cyclic voltammetry, galvanostatic charge–discharge and electrochemical impedance spectroscopy. The specific capacitance of the synthesized samples was obtained from the galvanostatic charge–discharge curves with the help of the equation as follows;

$$C_{sp} = \frac{I \times \Delta t}{m \times \Delta V} \tag{1}$$

where I, Δt, m and ΔV retain the usual meaning of input current in A, the discharge time in seconds, the mass load in grams and the operating potential window respectively.

3. Results and discussion

3.1. Characterisation of Fe doped ZnO nanomaterials

X-ray diffraction patterns of as synthesised Fe doped ZnO nanomaterials as shown in Fig. 1(a) displays intense and sharp peaks indicating the high crystalline nature. All the diffraction peaks are in good agreement with the wurtzite crystal structure of ZnO (ICDD 36-1451) belongs to the $P6_3mc$ space group of hexagonal symmetry (Fig. S5). There are no secondary or impurity phases were detected indicating retaining hexagonal wurtzite structure of ZnO nanomaterials. The average crystallite size is estimated using Scherrer equation $d = k\lambda/\beta\cos\theta$, where d is the mean crystallite size of nanomaterials, k is constant equal to 0.9, λ is the wavelength of X-ray used equal to 1.5406 Å,

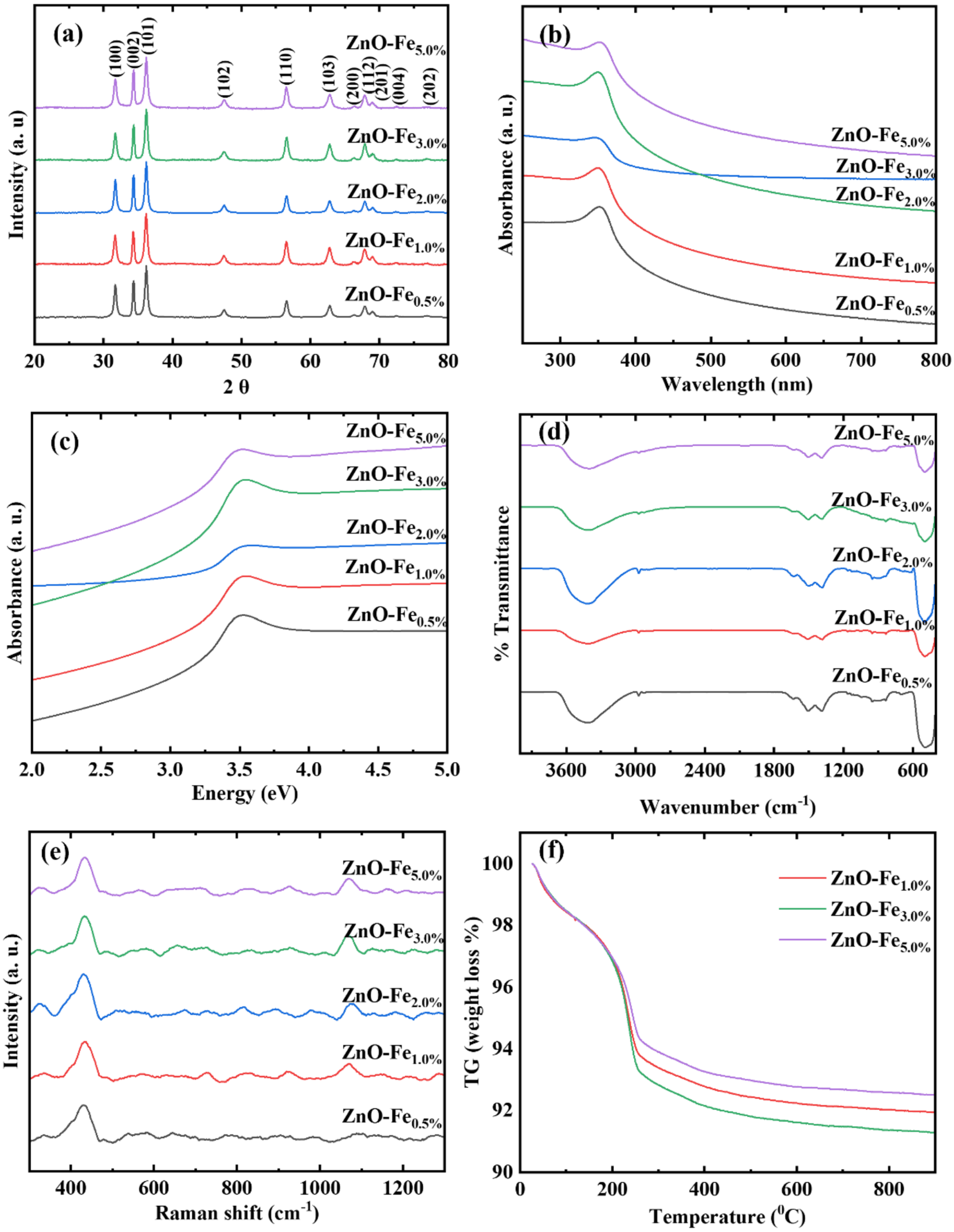

Fig. 1 (a) XRD patterns, (b) UV–vis absorption, (c) absorbance as a function of the optical excitation energy, (d) Fourier Transform Infra-Red (FT-IR) spectra, (e) Raman spectra and (f) thermogravimetric analysis (TGA) spectra of Fe doped ZnO nanomaterials.

Table 1 The lattice parameters of Fe doped ZnO nanomaterials

Compound name	Crystallite size in nm	$a = b$ (in Å)	c (in Å)	Unit cell volume (Å^3)
ZnO–Fe$_{0.5\%}$	18.58	3.249	5.207	47.33
ZnO–Fe$_{1.0\%}$	18.813	3.265	5.200	48.00
ZnO–Fe$_{2.0\%}$	17.47	3.247	5.206	47.42
ZnO–Fe$_{3.0\%}$	21.23	3.280	5.200	48.44
ZnO–Fe$_{5.0\%}$	21.226	3.280	5.200	48.44

β is the full width at half maximum (FWHM) of the diffraction peak in radian and θ is Bragg angle. It is observed that the crystallite size of Fe–ZnO nanomaterials increased when concentration of Fe increased from 2% to 3%. Distance between the Bragg's plane is calculated using Bragg's equation ($2d\sin\theta = n\lambda$), where d is distance between Bragg's plane, λ is the wavelength of incident beam, θ is the diffraction angle and n is the order of diffraction. The lattice parameters (a and c) tabulated in Table 1 were calculated using following eqn (2)

$$\frac{1}{d^2} = \frac{4}{3}\left(\frac{h^2 + hk + k^2}{a^2}\right)\frac{l^2}{c^2} \tag{2}$$

where d is distance between the Bragg's plane, h, k and l are the Miller indices, a and c are lattice cell constants. The unit cell volume (V) estimated using equation $V = 0.866a^2c$, where a and c are lattice cell constants.[32]

The optical properties of Fe doped ZnO nanomaterials were analysed using UV–vis as a function of wavelength, as shown in Fig. 1(b), Fe doped ZnO exhibits clear and narrow excitonic peaks in ultraviolet region (345 nm to 354 nm) which are attributed to electron transition from the valence band to the conduction band ($O_{2p} \rightarrow Zn_{3d}$),[35] and absorption decreases gradually in visible region. The absorption maximum shifts to lower wavelength as compared to pure ZnO nanomaterial synthesised using the same method in our previous work,[28] which shows absorption maximum at 367 nm. The observed blue shift in Fe doped zinc oxide is attributed to interaction of sp-d electrons of ZnO with the localised d electrons of Fe ion.[36] Band gap energy was determined using absorbance *versus* energy curve as shown in Fig. 1(c), the excitonic peaks at 3.52, 3.55, 3.59, 3.53 and 3.50 eV observed for ZnO–$Fe_{0.5\%}$, ZnO–$Fe_{1.0\%}$, ZnO–$Fe_{2.0\%}$, ZnO–$Fe_{3.0\%}$, and ZnO–$Fe_{5.0\%}$ Fe respectively, the observed change in band gap upon addition of iron ions in lattice sites of Zn^{2+} which provides addition free carriers causing Fermi level to move into conduction band.[37,38]

The FTIR spectra of Fe doped ZnO exhibited expected spectra of ZnO nanomaterials, a broad vibration band centred near 3400 cm^{-1} is associated to stretching vibration modes of O–H adsorbed from environment,[39] vibration bands centred around 2910 cm^{-1} is assigned to C–H stretching vibrations of CH_2 group, the bands centred around 1630 cm^{-1} are due to the O–H bending modes of vibrations,[40] bands centred around 1500 cm^{-1} and 1383 cm^{-1} are assigned to presence of carbonyl group[22] as seen in Fig. 1(d). The above-mentioned vibration bands could be absorbed by the nanomaterial's surface from the reaction medium or by exposure of the nanomaterials to an air atmosphere. Furthermore, the inorganic vibrational frequency of Zn–O nanomaterials is observed below 700 cm^{-1},[40] which is located around 480 cm^{-1}; the vibrational modes responsible for the iron oxide phase are not observed, which is in good agreement with XRD data. Raman spectroscopic analysis was conducted on Fe-doped ZnO nanoparticles across various concentrations (ranging from 0.5% to 5%). The resulting Raman spectra as shown in Fig. 1(e) for all concentrations exhibit nearly identical patterns with multiple vibration modes with slight peak shift which is attributed to structural defects and lattice distortion on doping in the crystals.[33] among all the peaks in Raman spectra, a distinct high intensity peak around 450 cm^{-1} attributed to intense non-polar optical vibration mode E_2 and low intense peak around 1070 cm^{-1} is assigned to acoustic combination of A1 and E2 vibration modes.[34] The similarity in the Raman spectra strongly suggests that the doping process does not significantly affect the core structure of the ZnO nanoparticles. Furthermore, variations in dopant concentration up to 5% do not induce notable structural changes, as further corroborated by X-ray diffraction (XRD) and microscopic studies.

Thermal stability of as synthesised Fe doped ZnO nanomaterials were accessed using Thermo gravimetric analysis (TGA), TG curve shown in Fig. 1(f) reveals thermal stability of Fe doped ZnO nanomaterials up to 900 °C, with minimum mass loss attributed to moisture loss, which is in agreement with presence of vibrational mode centred near 3400 cm^{-1} in FT-IR spectra. The observed thermal stability of Fe–ZnO nanomaterials aligns with the thermal stability of undoped ZnO nanomaterials reported in our previous work,[27] hence doping of ZnO with Fe has not impacted thermal stability of the synthesised nanomaterials. The XPS spectra were recorded for the representative Fe-doped ZnO nanoparticles to elucidate their elemental composition and chemical states. Fig. 2(a) presents the survey scan, which confirms the presence of key elements in the nanomaterial composite. The elements detected include zinc (Zn), iron (Fe), oxygen (O) and carbon (C) indicative of the successful synthesis and doping process. Carbon correction was performed to ensure accurate binding energy measurements and the corresponding high-resolution scans for individual elements are shown in Fig. 2(b–e). The high-resolution spectrum of carbon (C 1s) shown in Fig. 2(b) reveals a carbon peak attributed adventitious carbon contamination due to exposure of nanomaterials in air atmosphere[41] or carbon adsorbed by the nanomaterial's surface from reaction medium during the synthesis process, binding energy values observed for C 1s peak is 284.6, which is referenced to graphitic carbon.[22] The binding energy peak at 289.2 eV is attributed to the carboxyl carbon from the Zinc acetylacetonate hydrate precursor used during synthesis of the nanomaterial.

The high-resolution Zn 2p spectrum, Fig. 2(c) displays two prominent peaks, Zn $2p_{3/2}$ peak at 1021.27 eV and the Zn $2p_{1/2}$ peak at 1044.27 eV. The binding energy difference (Δ) of 23.00 eV between these two peaks is consistent with the literature values for ZnO, confirming the formation of zinc oxide. Additionally, the Zn $2p_{3/2}$ peak at 1021.27 eV aligns with Zn in the ZnO matrix, substantiating its oxidation state as Zn^{2+}.[42] This peak also excludes significant contributions from metallic Zn (0), reinforcing that ZnO has formed from the Zn precursor salt. The observed binding energy and peak separation validate the incorporation of Zn in the oxide lattice. Fig. 2(d) shows the peak of O 1s at 531.04 eV attributed to lattice oxygen.[43] To further substantiate the formation of Fe doped ZnO nanomaterials and to elucidate the oxidation state of iron, a high-resolution scan for the Fe 2p region was performed Fig. 2(e). Two distinct peaks are observed for Fe $2p_{3/2}$ peak at 710.87 eV and the Fe $2p_{1/2}$ peak at 724.64 eV, with a binding energy separation (Δ) of 13.77 eV. This Δ value is characteristic of Fe in its oxidized state and confirms the successful incorporation of iron into the ZnO matrix. The Fe $2p_{3/2}$ peak at 710.87 eV specifically indicates the presence of Fe^{3+},[44] corroborating that iron exists in its oxide form within the doped ZnO nanoparticles. This oxidation state is critical for understanding the electronic structure and potential applications, especially in electrochemical systems. The presence of iron in this state suggests its potential to enhance the catalytic and electronic properties of ZnO, making these composites suitable for advanced functional applications.

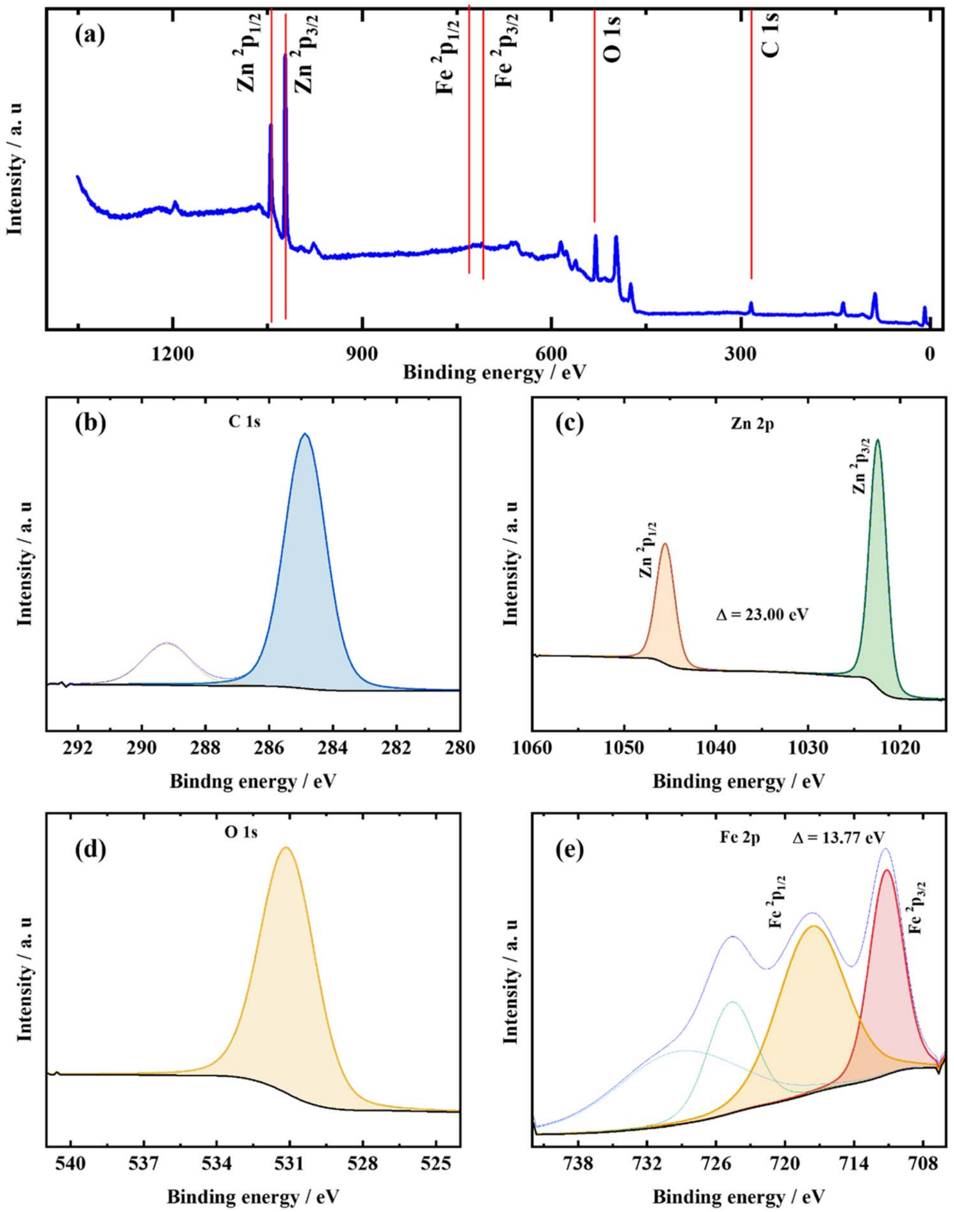

Fig. 2 (a) XPS survey spectra ZnO–$Fe_{5.0\%}$ nanomaterials and high-resolution spectra of (b) C 1s, (c) Zn 2p, (d) O 1s, (e) Fe 2p.

The surface morphology and elemental composition of the Fe-doped ZnO nanomaterials were investigated using field emission scanning electron microscopy (FESEM) coupled with energy-dispersive X-ray spectroscopy (EDX), and the results are presented in Fig. S1. The FESEM micrographs of all compositions—ZnO–$Fe_{0.5\%}$, ZnO–$Fe_{1.0\%}$, ZnO–$Fe_{2.0\%}$, ZnO–$Fe_{3.0\%}$, and ZnO–$Fe_{5.0\%}$—reveal an irregular, agglomerated particle morphology that is characteristic of sonochemically synthesized ZnO nanostructures, consistent with our previous reports. The particles display a rough, porous surface texture with no well-defined faceting across all doping concentrations, a feature that is electrochemically favorable as it provides an increased number of accessible active sites for electrolyte ion adsorption and charge transfer at the electrode–electrolyte interface, thereby contributing to the observed capacitive performance. No significant morphological transformation is observed as a function of increasing Fe doping concentration, indicating that the sonochemical synthesis protocol effectively preserves the inherent ZnO nanostructure architecture even at the highest doping level of 5.0 wt%. This morphological stability further confirms that Fe doping at the investigated concentrations does not induce the formation of discrete secondary iron oxide phases or promote particle sintering, which is fully consistent with the absence of impurity peaks in the XRD patterns. The EDX spectra recorded for all samples confirm the exclusive presence of Zn, O, and Fe signals with no detectable impurity elements, unambiguously validating the compositional purity of the synthesized nanomaterials and confirming that Fe is successfully introduced into the ZnO matrix across all doping concentrations investigated in this study.

Transmission Electron Microscopy (TEM) and High-Resolution Transmission Electron Microscopy (HRTEM) studies were conducted on Fe-doped ZnO nanoparticles to investigate their morphological characteristics, particle size distribution, and elemental composition. As illustrated in Fig. 3(a, c, e, g and i), the nanomaterials exhibited a monodisperse distribution across all tested concentrations of Fe doping, with minimal to no aggregation observed. This uniformity in particle distribution is a critical factor in determining the material's properties and performance in various applications. In addition to imaging, the TEM analysis included compositional and elemental distribution studies. Energy-Dispersive X-ray Spectroscopy (EDS) plots, presented in Fig. S2, confirmed the presence of Zn, O, and Fe peaks, providing clear evidence of the successful incorporation of Fe into the ZnO matrix. The rigorous washing and purification steps employed during sample preparation ensure that the detected Fe is not present as a surface impurity but is structurally integrated into the ZnO lattice. This finding is significant, as it underscores the intentional and controlled doping of Fe into the ZnO structure. To further elucidate the distribution and concentration of Fe within the ZnO matrix, elemental mapping studies were performed. The resulting images, displayed in Fig. S3, reveal a distinct increase in Fe distribution as the doping concentration rises to 5%. This trend unequivocally confirms the structural integration of Fe into the ZnO lattice and demonstrates that higher Fe concentrations in the reaction directly correlate with increased Fe incorporation into the matrix. This relationship is particularly important in the context of super capacitance analysis, where the doping level can significantly influence the material's electrochemical properties. Moreover, the inter planar spacing (d-values) was calculated from the lattice fringes observed in HRTEM images, as shown in Fig. 3(b, d, f, h and j). These d-values were found to be in close agreement with those obtained from X-ray Diffraction (XRD) analysis, further validating the crystallographic integrity of the Fe-doped ZnO nanoparticles. The consistency between TEM and XRD results reinforces the reliability of the structural and compositional data, providing a comprehensive understanding of the material's properties.

The selected area electron diffraction (SAED) patterns of Fe-doped ZnO nanoparticles were recorded using high-resolution transmission electron microscopy (HRTEM). The indexed diffraction patterns are presented in Fig. S4. These patterns exhibit a characteristic ring structure interspersed with bright spots along the rings, indicative of the sample's polycrystalline nature. The calculated d-values were subsequently used to assign Miller indices (*hkl*) to the corresponding planes. A comparison of these d-values with those obtained from X-ray diffraction (XRD) analysis revealed excellent agreement. Consequently, the assigned *hkl* planes derived from the SAED patterns were consistent with those identified through XRD, validating the crystallographic findings.

This analysis confirms that the Fe-doped ZnO nanomaterials synthesized in this study are indeed crystalline. The observed d-values and (*hkl*) indices align well with literature-reported values for polycrystalline ZnO, reinforcing the reliability of the structural determination. Furthermore, the incorporation of Fe into the ZnO lattice, at the investigated doping concentration, appears to have minimal impact on the crystal structure. This suggests that Fe doping, at low levels, does not significantly alter the hexagonal wurtzite structure of ZnO. These results provide strong evidence that the synthesized Fe-doped ZnO nanoparticles maintain their inherent crystalline properties, consistent with polycrystalline ZnO nanomaterials reported in the literature. Overall, the TEM and HRTEM studies, complemented by EDS and elemental mapping, provide a detailed

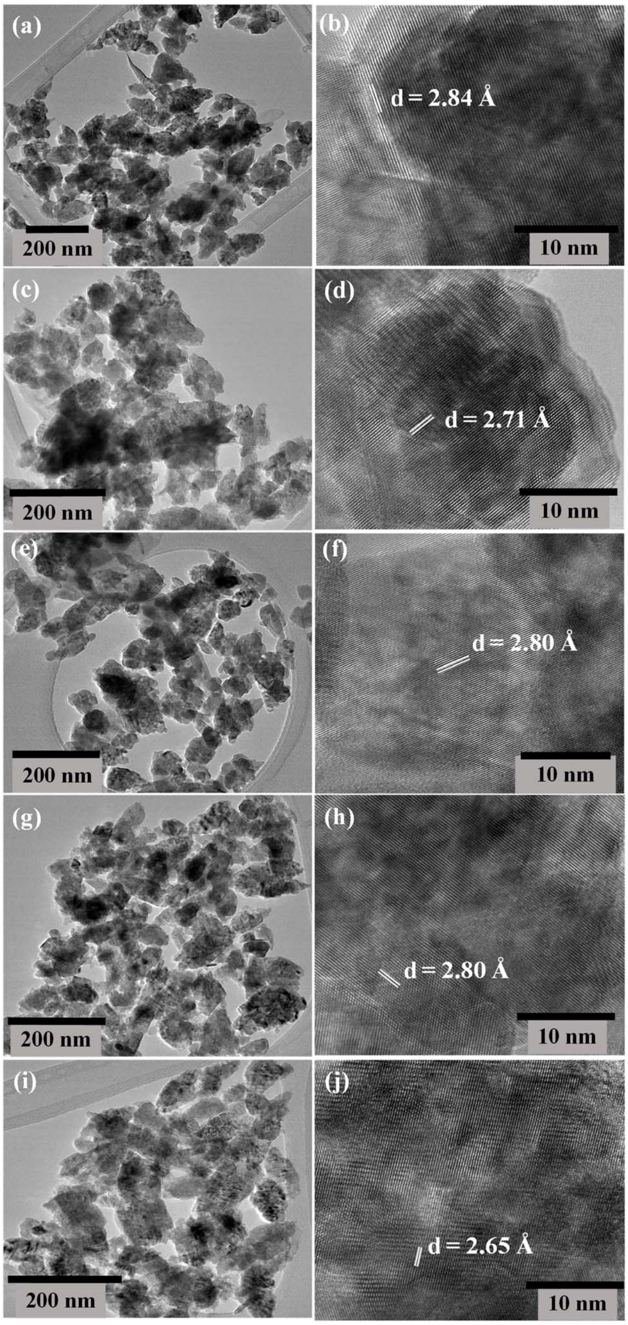

Fig. 3 TEM and HRTEM images of ZnO–Fe$_{0.5\%}$ (a and b), ZnO–Fe$_{1.0\%}$ (c and d), ZnO–Fe$_{2.0\%}$ (e and f), ZnO–Fe$_{3.0\%}$ (g and h) and ZnO–Fe$_{5.0\%}$ (i and j) nanomaterials.

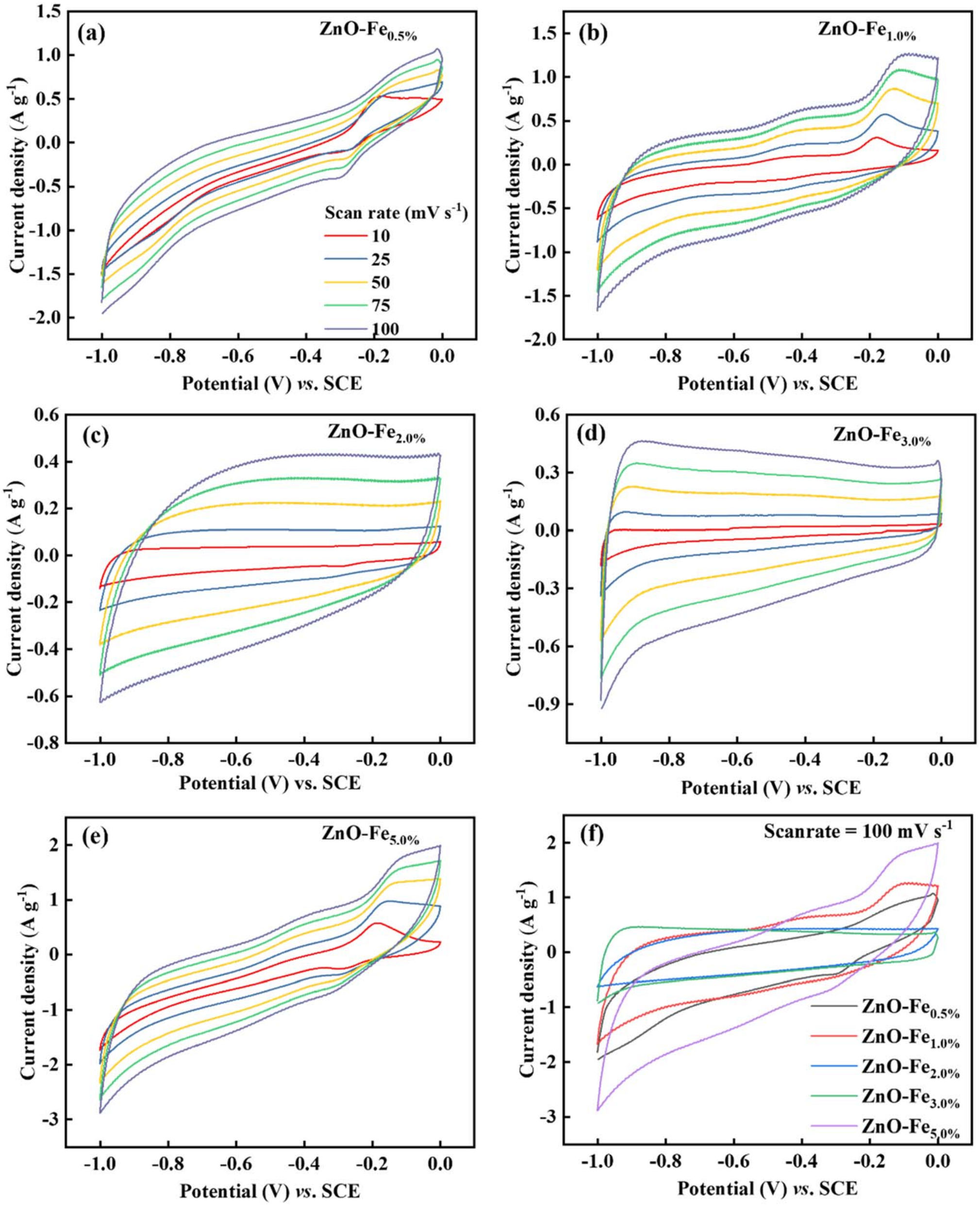

Fig. 4 Cyclic voltammogram of (a) ZnO–$Fe_{0.5\%}$, (b) ZnO–$Fe_{1.0\%}$, (c) ZnO–$Fe_{2.0\%}$, (d) ZnO–$Fe_{3.0\%}$, (e) ZnO–$Fe_{5.0\%}$ and (f) the comparison CV curve at scan rate of 100 mV s^{-1}.

insight into the morphology, particle distribution, and elemental composition of Fe-doped ZnO nanoparticles. These findings highlight the successful incorporation of Fe into the ZnO matrix and its impact on the material's structural and functional characteristics, which are crucial for applications such as supercapacitors.

3.2. Electrochemical investigation in a three-electrode system

The synthesized materials were taken up for electrochemical investigation in a three-electrode set-up in 3 M KOH. The active material slurry was applied to a 1 cm × 1 cm cross-sectional area of the Ni foam electrode surface. After coating, the electrode was dried in the oven for 60 °C. The mass loading of the active material was determined by measuring the weight of the Ni foam electrode before and after coating. The mass of the active material per unit area (mg cm^{-2}) was calculated based on the weight difference. The mass loading values for the different samples were calculated to be ZnO–$Fe_{0.5\%}$ = 12 mg cm^{-2}, ZnO–$Fe_{1.0\%}$ = 13.3 mg cm^{-2}, ZnO–$Fe_{2.0\%}$ = 11.2 mg cm^{-2}, ZnO–$Fe_{3.0\%}$ = 10.1 mg cm^{-2}, ZnO–$Fe_{5.0\%}$ = 12.0 mg cm^{-2}. The cyclic voltammetry experiments were conducted in the potential window of −1.0 to 0 V at varying scan rates from 10.0 mV s^{-1} to 100.0 mV s^{-1} as seen from Fig. 4. The plot of current *vs.* voltage for the CV exhibits a quasi-rectangular shape with redox shoulder peaks, indicating a combination of electric double-layer capacitance (EDLC) and pseudo capacitive behaviour.

The presence of redox shoulder peaks suggests that Fe doping induces faradaic redox reactions, enhancing the pseudocapacitive contribution. We could observe that at 0.5% Fe doping, the CV curve exhibits a well-defined shape with appreciable area, indicating good charge storage as seen from Fig. 4. At 1.0% and 2.0% Fe doping the redox peaks become more pronounced, implying an increased pseudocapacitive contribution. At higher Fe doping levels (3.0% and 5.0%), the CV curve becomes more resistive, with a less pronounced increase in the enclosed area. This suggests that excess Fe doping introduces charge-transfer resistance and possibly reduces the available active sites, negatively impacting performance.[45] Fig. 4(c) demonstrates the impact of varying Fe concentrations on the Electric Double Layer Capacitor (EDLC) characteristics of the ZnO–Fe composites. As the Fe content increases, a significant improvement in capacitive performance is observed, reflected in the rising current density across different scan rates. This improvement is attributed to the role of Fe in enhancing charge storage capacity and electrical conductivity. The interaction between Fe ions and the ZnO matrix likely creates a more favorable electrochemical environment, facilitating better ion diffusion and the formation of the electric double layer at the electrode interface. These results underscore the beneficial effects of Fe doping on the electrochemical properties, particularly in enhancing EDLC behavior, making it a promising approach for developing efficient energy storage devices. The supercapacitor behaviour of Fe-doped ZnO transitions from a dominant EDLC-type (at low Fe content) to a pseudocapacitive

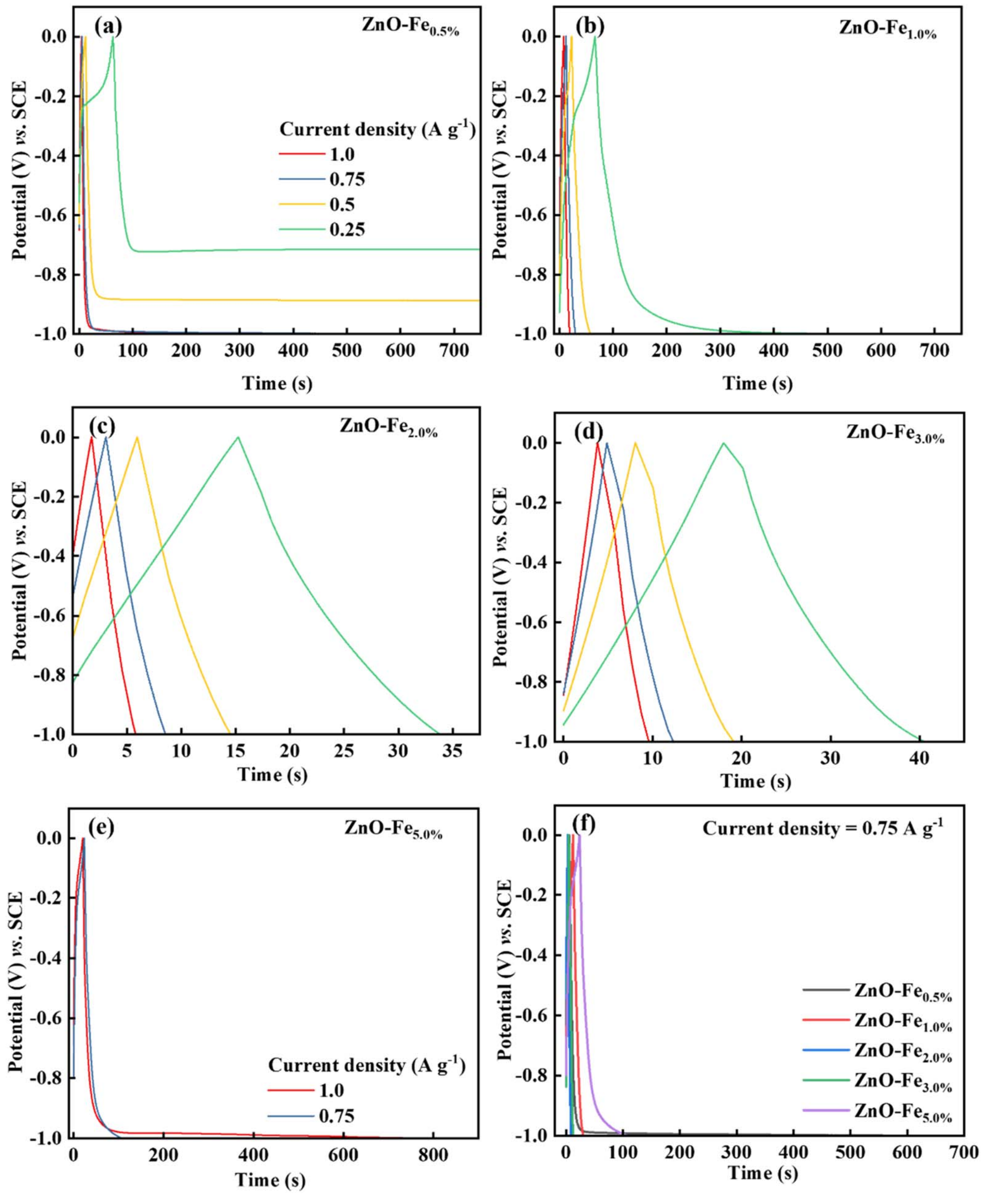

Fig. 5 GCD curves of (a) ZnO–$Fe_{0.5\%}$, (b) ZnO–$Fe_{1.0\%}$, (c) ZnO–$Fe_{2.0\%}$, (d) ZnO–$Fe_{3.0\%}$, (e) ZnO–$Fe_{5.0\%}$ and (f) comparison GCD curve at current density of 0.75 A g^{-1}.

mechanism with increasing Fe concentrations. At low doping levels (0.5%), Fe introduces beneficial redox-active sites, enhancing the charge storage capability.[23] However, beyond 1.0%, excessive Fe can lead to agglomeration, reduced electroactive surface area, and increased charge transfer resistance. Thus, implying that moderate Fe doping (~0.5%) is ideal for optimizing the electrochemical performance of ZnO-based supercapacitors.

The galvanostatic charge–discharge was carried out for the synthesized samples at the same potential window in different current densities ranging from 1.0 A g^{-1} to 0.25 A g^{-1} as depicted in Fig. 5. In an ideal supercapacitor, the GCD curve should be symmetric and triangular, indicating pure EDLC behaviour with negligible resistance and ideal charge–discharge characteristics. However, in the case of 0.5% Fe-doped ZnO, the GCD curve deviates from a perfect triangular shape as seen from Fig. 5(a). The ZnO–Fe exhibits redox activity, implying that the charge storage occurs not only *via* ion adsorption (EDLC behavior) but also through faradaic redox reactions.[46] The presence of Fe introduces redox-active sites, leading faradaic contribution, which distort the ideal triangular shape of an ideal supercapacitor.[47] From the comparison GCD curve at current density of 0.75 A g^{-1} as shown in Fig. 5(f), the specific capacitance values of Fe-doped ZnO varies significantly with Fe concentration, with ZnO–$Fe_{0.5\%}$ exhibiting highest capacitance of 462.0 F g^{-1} followed by ZnO–$Fe_{1.0\%}$ (12.0 F g^{-1}), ZnO–$Fe_{2.0\%}$ (3.0 F g^{-1}), ZnO–$Fe_{3.0\%}$ (4.5 F g^{-1}), and ZnO–$Fe_{5.0\%}$ (62.25 F g^{-1}). At 0.5% Fe doping level, Fe incorporation enhances electron transport and pseudocapacitive behaviour without disrupting the ZnO structure. However, as Fe doping increases beyond 1.0%, excessive defects and the formation of non-conductive Fe-based oxide phases hinder charge transfer, drastically reducing capacitance.[48] At 5.0% Fe doping, a slight recovery is observed in capacitance value (62.25 F g^{-1}) due to the formation of iron oxide nanoclusters contributing to redox activity. These results indicate that 0.5% Fe doping is optimal for maximizing supercapacitor performance.

The electrochemical impedance spectroscopy (EIS) analysis was carried out over a frequency range from 10^{-1} Hz to 10^{6} Hz for Fe-doped ZnO samples as shown in Fig. 6(a–e). The Nyquist plot reveals that the charge transfer resistance (R_{ct}) for ZnO–$Fe_{0.5\%}$ is the lowest (0.3 Ω), followed by ZnO–$Fe_{3.0\%}$ (0.77 Ω) and ZnO–$Fe_{5.0\%}$ (1.51 Ω), while ZnO–$Fe_{1.0\%}$ and ZnO–$Fe_{2.0\%}$ exhibit significantly higher resistance of 1.2 Ω and 16.29 Ω respectively.[49] The remarkably low R_{ct} of ZnO–$Fe_{0.5\%}$ suggests superior charge transfer kinetics, minimizing resistive losses and facilitating efficient ion-diffusion at the electrode–electrolyte interface.[50]

Among all the Fe-doped ZnO samples, the ZnO–$Fe_{0.5\%}$ electrode delivers the highest capacitance (426 F g^{-1}), which directly corresponds to its lowest charge-transfer resistance obtained from EIS fitting (as seen from Fig. 7(a–e). A small amount of Fe improves the electronic pathways and creates accessible defect sites, allowing faster charge transfer and easier ion movement through the electrode.[51] When the Fe content is increased beyond 0.5%, the R_{ct} rises and the capacitance drops sharply recorded as 12.0, 3.0, 4.5, and 62.25 F g^{-1} for 1%, 2%, 3%, and 5% Fe, respectively indicating that excessive doping leads to structural disorder, agglomeration, and blocked active sites. These effects hinder both electron transport and electrolyte diffusion.[52] Thus, 0.5% Fe provides the most favourable balance between conductivity, defect chemistry, and ion accessibility, making it the optimum composition for supercapacitor applications.

The trend in this R_{ct} is further supported by GCD and cyclic voltammetry (CV) results. The near-triangular shape of the GCD curve for ZnO–$Fe_{0.5\%}$ reflects ideal capacitive behaviour with minimal iR drop, confirming its efficient charge storage capability. Additionally, the CV curve exhibits a more rectangular profile compared to higher doping levels, indicating enhanced

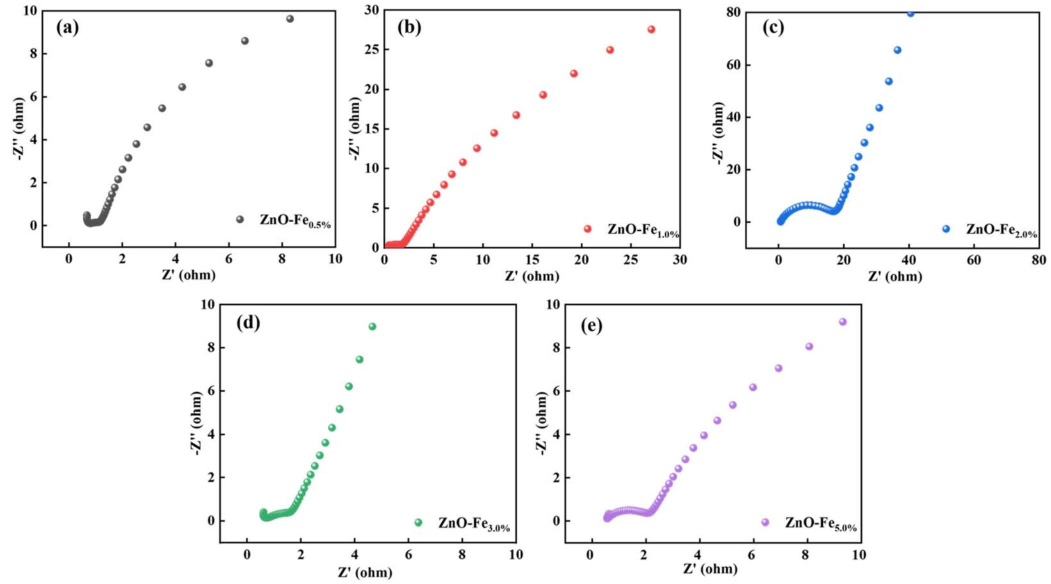

Fig. 6 EIS of (a) ZnO–$Fe_{0.5\%}$, (b) ZnO–$Fe_{1.0\%}$, (c) ZnO–$Fe_{2.0\%}$, (d) ZnO–$Fe_{3.0\%}$, (e) ZnO–$Fe_{5.0\%}$.

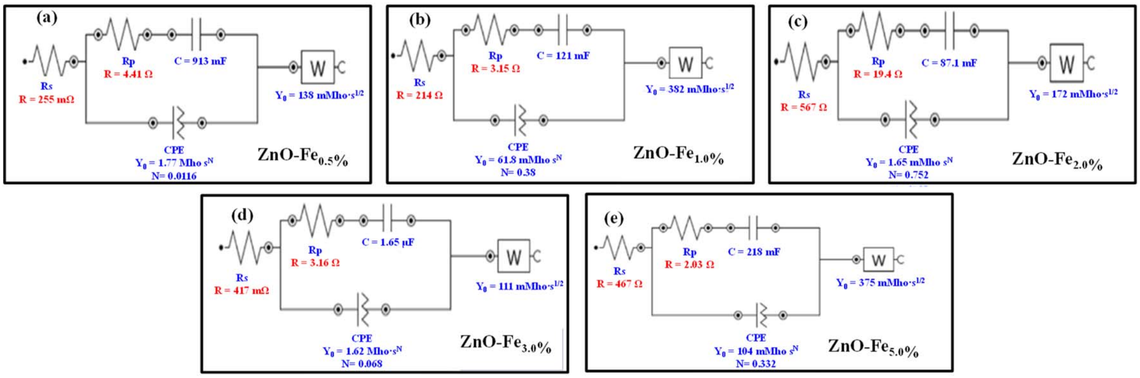

Fig. 7 Electrochemically fitted circuit for (a) ZnO–$Fe_{0.5\%}$, (b) ZnO–$Fe_{1.0\%}$, (c) ZnO–$Fe_{2.0\%}$, (d) ZnO–$Fe_{3.0\%}$, (e) ZnO–$Fe_{5.0\%}$.

electrochemical reversibility and superior charge–discharge stability. In contrast, increased Fe doping (1.0%–5.0%) disrupts ZnO's conductivity, introducing excessive defects and charge recombination sites, leading to reduced electrochemical performance. Therefore, ZnO–$Fe_{0.5\%}$ emerges as the optimal doping concentration for enhanced supercapacitor applications. A comprehensive comparison is made between recently published work on the supercapacitor performance of doped ZnO nanomaterials and the Fe doped ZnO nanomaterial (present work) as shown in Table 2, it is evident that there is significant increase in the specific capacitance on ZnO nanomaterials doped with Fe.

3.3. Electrochemical behaviour of ZnO–Fe in two-electrode system

After initial three-electrode screening, ZnO–$Fe_{0.5\%}$ demonstrated superior capacitance, and hence was further evaluated in a symmetric two-electrode configuration, where ∼6 mg of active material was coated on the cathode and slightly more on the anode to compensate for charge imbalance. So, a symmetric supercapacitor device was fabricated in a coin cell configuration. In the case of ZnO modified with 0.5% Fe, the incorporation of Fe ions into the ZnO lattice introduces additional redox-active sites (Fe^{2+}/Fe^{3+}), enhances electron transport pathways, and generates lattice defects that improve ion diffusion kinetics. During charging, electrolyte cations and anions migrate towards the negatively and positively polarized ZnO–Fe electrodes, respectively. At the negative side rapid surface adsorption as well as partial faradaic contributions from Fe centre take place and ion desorption followed by electron release takes place during discharge process maintaining high reversibility and cycle stability. The charge–discharge mechanism is governed by the fast and reversible adsorption/desorption of electrolyte ions at the electrode–electrolyte interface, combined with faradaic redox reactions provided by transition-metal doping. So, the combined effect of capacitive and faradaic charge storage mechanism results in quasi-rectangular CV profiles and nearly triangular GCD curves at different current densities. The GCD measurements (Fig. 7(a)) at different current densities (0.1, 0.2, 0.5, 1, and 2 A g^{-1}) exhibited stable voltage-time profiles with minor IR drops, confirming the efficient charge storage and rapid ion transport within the electrode structure. Correspondingly, the Ragone plot (Fig. 7(b)) revealed energy densities of 3.3, 1.7, 2.1, 2.3, and 1.6 Wh kg^{-1} at power densities of 142.6, 288.61, 716.7, 1436.7, and 2890.93 W kg^{-1},respectively, demonstrating a favourable trade-off between

Table 2 Specific capacitance comparison for ZnO doped with different elements and Fe doped ZnO nanomaterials in the present work

Electrode material	Electrolyte	Specific capacitance (F g^{-1})	Current density (A g^{-1}) or scan rate (mV s^{-1})	References
ZnO–Nd	2 M KOH	25	2.5 A g^{-1}	14
ZnO–Mo	2 M KOH	336	0.5 A g^{-1}	15
ZnO–V	2 M KOH	362	0.5 A g^{-1}	15
ZnO–Au	2 M KOH	205	10 mV s^{-1}	16
ZnO–Ni	0.5 M Na_2SO_4	95.32	10 mV s^{-1}	17
ZnO–Mn	3 M KOH	220	10 mV s^{-1}	18
ZnO–Mn	6 M KOH	86	0.15 A g^{-1}	19
ZnO–Cu	6 M KOH	86.6	0.15 A g^{-1}	19
ZnO–Ni	2 M KOH	133	10 mV s^{-1}	20
ZnO–Li	2 M KOH	125	10 mV s^{-1}	21
ZnO–Cr	6 M KOH	163.3	1 A g^{-1}	22
ZnO–Cr/Fe	6 M KOH	255.3	1 A g^{-1}	22
ZnO–Cr/Co	6 M KOH	337.9	1 A g^{-1}	22
ZnO–Cr/Mg	6 M KOH	209.1	1 A g^{-1}	22
ZnO–Fe	1 M KOH	276.4	1 A g^{-1}	23
ZnO–Fe	3 M KOH	462.0	0.75 A g^{-1}	Our work

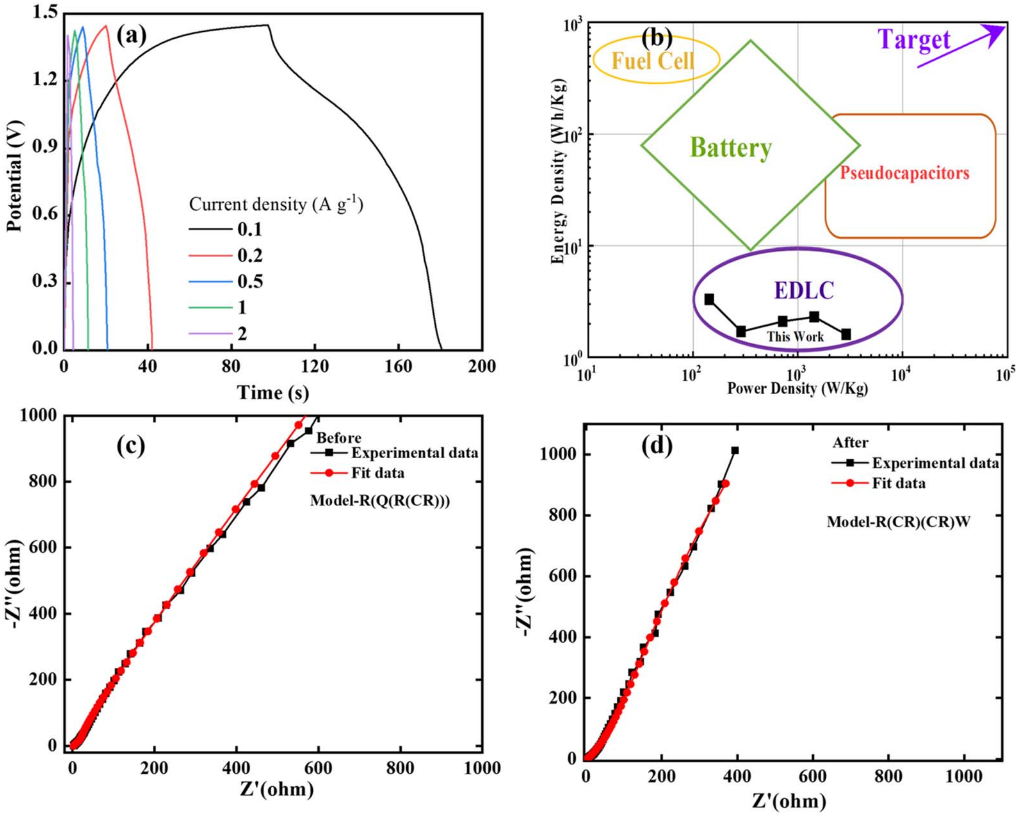

Fig. 8 (a) GCD characteristics of ZnO–$Fe_{0.5\%}$, in 2-electrode set up (b) mapping of device in Ragone plot indicating superior power density than batteries, (c) EIS before and (d) EIS after GCD along with equivalent circuit fit.

energy and power delivery. These results highlight that the Fe-modified ZnO electrode not only provides high capacitance at low current densities but also maintains excellent rate performance and stability under high current operation, establishing ZnO–$Fe_{0.5\%}$ as a promising electrode material for next-generation supercapacitor applications. Electrochemical impedance measurements were recorded (Fig. 8(c and d)) before and after GCD studies. The cell showed a solution resistance of 2.7 and 2.4 Ω before and after GCD respectively indicating minimal internal cell resistance. Nyquist plot also shows a steep slope indicating the capacitive behaviour of the cell.

4. Conclusion

This present study reports the preparation and detailed evaluation of Fe-doped ZnO nanostructures for use in supercapacitor electrodes. Introducing Fe into the ZnO lattice produced clear modifications in crystallinity, surface morphology, and optical behaviour, as confirmed through XRD, SEM, TEM and UV–vis analyses. Among the investigated samples, the ZnO–$Fe_{0.5\%}$ electrode showed the most promising charge-storage ability (11.4 F g^{-1}), indicating that a small amount of Fe effectively promotes defect formation and redox activity that support improved electrochemical performance. The material also maintained stable behaviour during repeated cycling, highlighting its reliability as an electrode. Overall, the results demonstrate that tuning dopant concentration is a practical approach for tailoring the properties of ZnO for energy-storage applications. Further studies focusing on optimized Fe loading, hybrid electrode design and mechanistic understanding could help advance ZnO-based supercapacitors.

Author contributions

Srikanth R. Veerabhadraiah: writing – original draft, methodology, investigation, formal analysis, data curation, validation, conceptualization, Gowri Soman: writing – original draft, investigation, formal analysis, Sachin A. Bhat: writing – original draft, formal analysis, data curation. Rohit K. Sharma: investigation, formal analysis, Ravi kumar Thimmappa: investigation, formal analysis, Chinmaya Mirle: validation, data curation, Gurumurthy Hegde: writing – review & editing, investigation, conceptualization, supervision, C. V. Yelamaggad: investigation, formal analysis, Nagaraja Naik: validation, conceptualization, supervision.

Conflicts of interest

There are no conflicts to declare.

Data availability

The data supporting the findings of this study are available within the article and its supplementary information (SI).

Supplementary information is available. See DOI: https://doi.org/10.1039/d6ra02336c.

Acknowledgements

The authors gratefully acknowledge Centre for Nano and Soft Matter Sciences (CeNS), Bengaluru for instrumentation facility. Authors acknowledge Dr Thomas Diemant from Helmholtz Institute Ulm (HIU), Ulm, Germany, for recording and providing XPS data.

References

1 T.-Z. Ang, M. Salem, M. Kamarol, H. S. Das, M. Alhuyi Nazari and N. Prabaharan, *Energy Strategy Rev.*, 2022, **43**, 100939.
2 D. A. Elalfy, E. Gouda, M. Fawzi Kot, V. Bureš and B. E. Sedhom, *Energy Strategy Rev.*, 2024, **54**, 101482.
3 Q. Wu, T. He, Y. Zhang, J. Zhang, Z. Wang, Y. Liu, L. Zhao, Y. Wu and F. Ran, *J. Mater. Chem. A*, 2021, **9**, 24094.
4 D. P. Chatterjee and A. K. Nandi, *J. Mater. Chem. A*, 2021, **9**, 15880.
5 S. Liu, L. Wei and H. Wang, *Appl. Energy*, 2020, **278**, 115436.
6 A. G. Olabi, Q. Abbas, A. Al Makky and M. A. Abdelkareem, *Energy*, 2017, **248**, 123617.
7 L. Guo, P. Hu and H. Wei, *J. Energy Storage*, 2023, **65**, 107269.
8 K. Dissanayake and D. Kularatna-Abeywardana, *J. Energy Storage*, 2024, **96**, 112563.
9 N. Kumar, S.-B. Kim, S.-Y. Lee and S.-J. Park, *Nanomaterials*, 2022, **12**, 20.
10 P. Bhojane, *J. Energy Storage*, 2022, **45**, 103654.
11 C. Yin, X. Guo, X. Qin, J. Shi, L. Jiang, Q. Li, M. Shakouri, B. He, H. Zhou, C. Ma and H. Pang, *Adv. Mater.*, 2026, **38**, e72860.
12 Z. Yang, H. Lu, Q. Li, X. Guo, Q. Li, H. Zhou, B. Wang, Y. Qi, H.-C. Chen, M. Yang, T. Tian, H. Yang, J. Ding and H. Pang, *Adv. Mater.*, 2026, **38**, e12289.
13 Ç. T. Altaf, Ö. Coşkun, A. Kumtepe, A. M. Rostas, I. Iatsunskyi, E. Coy, E. Erdem, M. Sankir and N. D. Sankir, *Sci. Rep.*, 2022, **12**, 11487.
14 J. Sahu, S. Kumar, F. Ahmed, P. A. Alvi, B. Dalela, D. M. Phase, M. Gupta and S. Dalela, *J. Energy Storage*, 2023, **59**, 106499.
15 M. R. Pallavolu, J. Nallapureddy, R. R. Nallapureddy, G. Neelima, A. K. Yedluri, T. K. Mandal, B. Pejjai and S. W. Joo, *J. Alloys Compd.*, 2021, **886**, 161234.
16 H. Mahajan, J. Bae and K. Yun, *J. Alloys Compd.*, 2018, **758**, 131.
17 I. N. Reddy, Ch. V. Reddy, A. Sreedhar, J. Shim, M. Cho, K. Yoo and D. Kim, *J. Electroanal. Chem.*, 2018, **828**, 124.
18 A. Rana, R. Malik, M. Rana, D. Kaushik, S. P. Khanna, R. Srivastava and C. K. Suman, *J. Alloys Compd.*, 2024, **997**, 174931.
19 A. U. Ammar, F. Bakan-Misirlioglu, M. H. Aleinawi, G. Franzo, G. G. Condorelli, F. N. T. Yesilbag, Y. O. Yesilbag, S. Mirabella and E. Erdem, *Res. Bull.*, 2023, **165**, 112334.
20 A. Mohan, V. Manikandan, S. Devanesan, M. S. AlSalhi, C. Rajeevgandhi, S. Guo and L. Guganathan, *Chemosphere*, 2022, **299**, 134366.
21 C. Rajeevgandhi, S. Bharanidharan, T. Jayakumar, N. Shailaja, P. Anand, L. Guganathan, P. Balasubhramanyam and C. A. Kumar, *Solid State Commun.*, 2023, **371**, 115256.
22 K. S. Kumar, M. A. Ghanem, L. Reddy, N. Roy and S. W. Joo, *Ceram. Int.*, 2024, **51**, 8634.
23 S. Kumar, F. Ahmed, N. M. Shaalan, N. Arshi, S. Dalela and K. H. Chae, *Nanomaterials*, 2023, **12**, 2222.
24 T. Srinivasulu, K. Saritha and K. T. R. Reddy, *Mod. Electron. Mater.*, 2017, **3**, 76.
25 M. A. Ciciliati, M. F. Silva, D. M. Fernandes, M. A. C. de Melo, A. A. W. Hechenleitner and E. A. G. Pineda, *Mater. Lett.*, 2015, **159**, 84.
26 A. Gedanken, and I. Perelshtein, Power ultrasound for the production of nanomaterials, in *Power Ultrasonics: Applications of High-Intensity Ultrasound*, ed. J. A. Gallego-Juárez and K. F. Graff, Woodhead, Cambridge, U.K., 2015, pp. 543–576.
27 S. R. Veerabhadraiah, S. A. Bhat, R. K. Sharma, C. V. Yelamaggad and N. Naik, *ChemistrySelect*, 2024, **9**, e202400617.
28 S. R. Veerabhadraiah, S. Maji and A. Panneerselvam, *J. Cryst. Growth*, 2022, **579**, 126430.
29 M. S. Ratsoma, B. L. O. Poho, K. Makgopa, K. Raju, K. D. Modibane, C. J. Jafta and K. O. Oyedotun, *J. Electron. Mater.*, 2023, **52**, 2264.
30 Z. Chen, H. Yang, X. Men, L. Yao, Q. Fu, Z. Lin and S. Wang, *J. Chem. Educ.*, 2022, **99**, 2715.
31 S. Gyawali, L. K. M. O. Goni, M. S. Chowdhury, A. Laref, S. Bajgai, S. Chantrapromma and K. Techato, *Mater. Res. Express*, 2022, **9**, 055004.
32 R. Torkamani and B. Aslibeiki, *J. Cryst. Growth*, 2023, **618**, 127317.
33 S. S. Ghosh, C. Choubey and A. Sil, *Superlattices Microstruct.*, 2019, **125**, 271.
34 N. Sebastian, W.-C. Yu, Y.-C. Hu, D. Balram and Y.-H. Yu, *Ultrason. Sonochem.*, 2019, **59**, 104696.
35 V. Kumar, H. C. Swart, M. Gohain, V. Kumar, S. Som, B. C. B. Bezuindenhoudt and O. M. Ntwaeaborwa, *Ultrason. Sonochem.*, 2014, **21**, 1549.
36 Y. B. S. Rao, D. Parajuli, M. V. S. Rao, A. Ramakrishna, K. Ramanjaneyulu, T. W. Mammo, P. S. V. Shanmukhi, M. S. N. A. Prasad, G. M. Rao, B. Suryanarayana and N. Murali, *Chem. Phys. Impact*, 2023, **7**, 100270.
37 P. Ariyakkani, L. Suganya and B. Sundaresan, *J. Alloys Compd.*, 2017, **695**, 3467.
38 L. Xu and X. Li, *J. Cryst. Growth*, 2010, **312**, 851.
39 G. Rytwo, R. Zakai and B. Wicklein, *J. Spectrosc.*, 2015, 727595.
40 F. F. H. Aragón, L. Villegas-Lelovsky, J. Parizaka, E. G. Zela, R. Bendezu, R. O. Gallegos, D. G. Pacheco-Salazar, S. W. da Silva, R. Cohen, L. C. C. M. Nagamine, J. A. H. Coaquira and P. C. Morais, *Mater. Adv.*, 2023, **4**, 1389.

41 J. T. Titantah and D. Lamoen, *Diamond Relat. Mater.*, 2007, **16**, 581.

42 S. Song, K. Wu, H. Wu, J. Guo and L. Zhang, *Dalton Trans.*, 2019, **48**, 13260.

43 X. Wu, Y. H. Ng, X. Wen, H. Y. Chung, R. J. Wong, Y. Du, S. X. Dou, R. Amal and J. Scott, *Chem. Eng. J.*, 2018, **353**, 636.

44 C. Han, L. Duan, X. Zhao, Z. Hu, Y. Niu and W. Geng, *J. Alloys Compd.*, 2019, **770**, 854.

45 R. Naik, *Chem. Phys. Impact*, 2023, 100387.

46 K. Sathiyamurthy, C. Rajeevgandhi, L. Guganathan, S. Bharanidharan and S. Savithiri, *J. Mater. Sci.: Mater. Electron.*, 2021, **32**, 11593.

47 C. K. Brozek, D. Zhou, H. Liu, X. Li, K. R. Kittilstved and D. R. Gamelin, *Nano Lett.*, 2018, **18**, 3297.

48 W. Guo, B. Zhao, Q. Zhou, Y. He, Z. Wang and N. Radacsi, *ACS Omega*, 2019, **4**, 10252.

49 A. Gurumukhi, *ChemRxiv*, 2024, preprint, DOI: 10.26434/chemrxiv-2024-mnf3b.

50 O. Baytar, A. Ekinci, S. Kutluay, G. Canpolat, Ö. Şahin and S. Horoz, *J. Aust. Ceram. Soc.*, 2024, **12**, 1697.

51 Y. Shao, Z. Mao, J. Wang, X. Hao, Y. Jia, Y. Xu and K. Sun, *ACS Appl. Energy Mater.*, 2025, **18**, 13808.

52 T. Putjuso, S. Putjuso, A. Karaphun, P. Moontragoon, I. Kotutha and E. Swatsitang, *Sci. Rep.*, 2023, **13**, 2531.